Electronic Supplementary Material (ESI) for Energy & Environmental Science.

A Bifunctional Solid State Catalyst with Enhanced Cycling Stability for Na and Li-O_2 Cells: Revealing the Role of Solid State Catalyst

Hossein Yadegari,[1,#] Mohammad Norouzi Banis,[1,2,#] Andrew Lushington,[1] Qian Sun,[1] Ruying Li,[1] Tsun-Kong Sham[3] and Xueliang Sun[1,*]

[1] Department of Mechanical and Materials Engineering, University of Western Ontario, London, Ontario N6A 5B9, Canada

[2] Canadian Light Source, Saskatoon S7N 2V3, Canada

[3] Department of Chemistry, University of Western Ontario, London, Ontario N6A 5B7, Canada

[*] Corresponding author: xsun@eng.uwo.ca

[#] Hossein Yadegari and Mohammad Norouzi Banis have equivalent contributions to this work.

Materials and Methods

Synthesis of Gr foam. Gr foam was synthesized using a chemical vapor deposition (CVD) technique previously reported.[1] The synthesis procedure is briefly described as follow: A piece of Ni foam (1.2 mm in thickness) was used as a self-sacrificing template and catalyst surface to grow graphene. Ni foam was cut into the desired dimensions and placed in a quartz tube. The quartz tube were transferred into a horizontal furnace and purged with Ar (500 sccm) and H_2 (50 sccm) for 15 min. The furnace was then heated up to 1000 °C and kept at this temperature for 15 min to remove the surface contaminants and oxide layer from Ni foam. CH_4 was then introduced into the tube as the carbon source at a flow rate of 0.5 sccm for 1 h. The sample was then cooled down to room temperature under flowing Ar and H_2. Afterward, the sample was placed in a 3 M HCl solution at 50°C overnight to completely dissolve Ni template.

Synthesis of Gr/NCNT. Gr/NCNT foam was synthesized using a modified spray pyrolysis chemical vapor deposition (SPCVD) method.[2] In a typical synthesis, Gr foam (with Ni template) was physically sputtered with a 30 nm of aluminum as the buffer layer and a 10 nm of iron as a CVD catalyst. The Fe catalyst applied for NCNT growth was physically sputtered on the Gr surface in a modified SPCVD method, in contrast to the conventional process where the catalyst was being sprayed on the desired surface.[2] The modified SPCVD method provides better control over NCNT density. The sputtered Gr foam was then fixed inside a quartz tube and transferred into a vertical furnace. The quartz tube was purged with Ar (500 sccm) for 15 min to produce an inert atmosphere. The furnace was then heated up to 850 °C and a solution containing 2 g of imidazole in 10 mL of acetonitrile was introduced into the tube with the aid of an ultrasonic probe sonicator at a flow rate of 250 µL/min for 10 min. The Ni template was consequently removed using the aforementioned etching procedure.

Synthesis of Gr/NCNT/MnO. Mesoporous Mn_3O_4 was synthesized on NCNT surface using a chemical precipitation method.[3] In a typical synthesis procedure, as-prepared Gr/NCNT sample were transferred into a solution containing $KMnO_4$ (10 mg/ml) and H_2SO_4 (5%) at 45 °C for 3 min. The Gr/NCNT/MnO was then transferred into cold distilled water to stop the reaction and washed several times using water and ethanol.

Synthesis of Gr/NCNT/MnO/Pd. The Pd catalyst was deposited using an Arradiance GEMstar-8 ALD system using alternating exposure of Pd(II) hexafluoroacetylacetonate, $Pd(hfac)_2$, and formalin at a processing pressure of 0.8 Torr. Both precursors were obtained from Sigma Aldrich and used as received. Formalin solution was composed of 37% formaldehyde in water containing 10-15% methanol to prevent polymerization. $Pd(hfac)_2$ was held in a stainless steel bubbler at 50°C to maintain a vapor pressure slightly less than 0.1 Torr. Manifold temperature was maintained at 100°C while deposition temperature was kept constant at 200°C. Ultrahigh purity nitrogen (99.999%) was used as a carrier gas and purge gas throughout the experiment with a mass flow of 20 sccm. ALD deposition can be expressed as t_1-t_2-t_3-t_4 where t_1 is the exposure time for the first precursor ($Pd(hfac)_2$) and t_2 is the purge time following the first precursor and t_3 and t_4 are second precursor pulse (formalin) and purge respectively. A timing sequence of 2-30-1-30 s was used for the deposition of Pd to produce the Gr/NCNT/MnO/Pd electrode.

Physical Characterizations. Morphological studies were performed by Hitachi S-4800 field-emission scanning electron microscope (SEM) and high-resolution TEM (HRTEM, JEOL 2010FEG) scanning transmission electron microscopy (STEM). N_2 adsorption/desorption isotherms were obtained using a Folio Micromeritics TriStar II 3020 Surface Area and Pore Size Analyzer. The surface area of the electrodes was calculated using a Brunauer, Emmett, and Teller (BET) model by taking at least six data points where $0.07 < P/P_0 < 0.2$. Pore size distribution was obtained by the Barrett, Joyner, and Halenda (BJH) model using the desorption branch of the isotherm. Thermogravimetric analysis (TGA) was performed using a SDT Q600 TGA unite from room temperature (RT) to 900 °C in air at a heating rate of 10 °C min^{-1}. Raman data was collected using a HORIBA Scientific LabRAM HR Raman spectrometer operated with an incident laser beam at 532.03 nm. X-ray diffractograms were obtained using a Bruker D8 Advance (Cu-Kα source, 40 kV, 40 mA). For the X-ray diffraction (XRD) measurements, the Na-O_2 cells were dissembled in an Ar-filled glovebox following electrochemical cycling, and the positive electrode materials were placed into an air-sensitive XRD sample holder. XAS measurements were obtained at the Canadian Light Source (CLS) on the spherical grating monochromator (SGM) and hard X-ray micro-analysis (HXMA) beamlines. In order to examine the discharge product of the cells, the discharged cells were dissembled inside a glovebox, the air electrodes were then sealed

transferred to the beamline end-station, where the samples were opened in a second glovebox and placed into the XAS vacuum chamber. The samples were kept under pure argon atmosphere before the analytical measurements, without any exposure to the atmospheric air. The vacuum during the XAS experiments was around 10^{-8} Torr.

Electrochemical Measurements. Swagelok-type cells composed of sodium foil anode, Celgard 3500 separator (5/8 in. in diameter), different air electrode, and a stainless steel mesh as current collector were used to carry out electrochemical measurements. The employed Swagelok cell configuration is described elsewhere.[2] The air electrodes were cut into circular pieces (3/8 in. in diameter) with the geometric surface area of 0.71 cm^2. The specific mass (loading) of the air electrodes were calculated based on the TGA results to be ~1.9, 2.0, 2.2 and 2.3 mg cm^{-2} for Gr/NCNT, Gr/NCNT/Pd-150C, Gr/NCNT/MnO and Gr/NCNT/MnO/Pd-150C electrodes, respectively. A fresh sodium or lithium foil (3/8 in. in diameter) was used as negative electrode material. The electrolyte used in this study was 0.5 M sodium or lithium triflate ($Na/LiSO_3CF_3$, Aldrich) dissolved in diethylene glycol diethyl ether (DEGDME, Anhydrous ≥ 99.5%, Aldrich). Sodium and lithium triflate electrolyte salt was dried at 80 °C under vacuum for 48 h, and the water content of DEGDME solvent was removed using molecular sieves (3 Å) for at least 10 days. The amount of electrolyte in the cell was ~200 µL. The assembled Na or Li-O_2 cells were placed into a homemade testing box inside the glovebox and then transferred to the testing room. The argon content of testing box was moderately vacuumed out and then pure oxygen (purity 5.0) was purged into the box. The pressure of testing box was kept at 1.0 atm during the electrochemical tests. Discharge/charge characteristics were performed using an Arbin BT-2000 battery station at RT (25 °C).

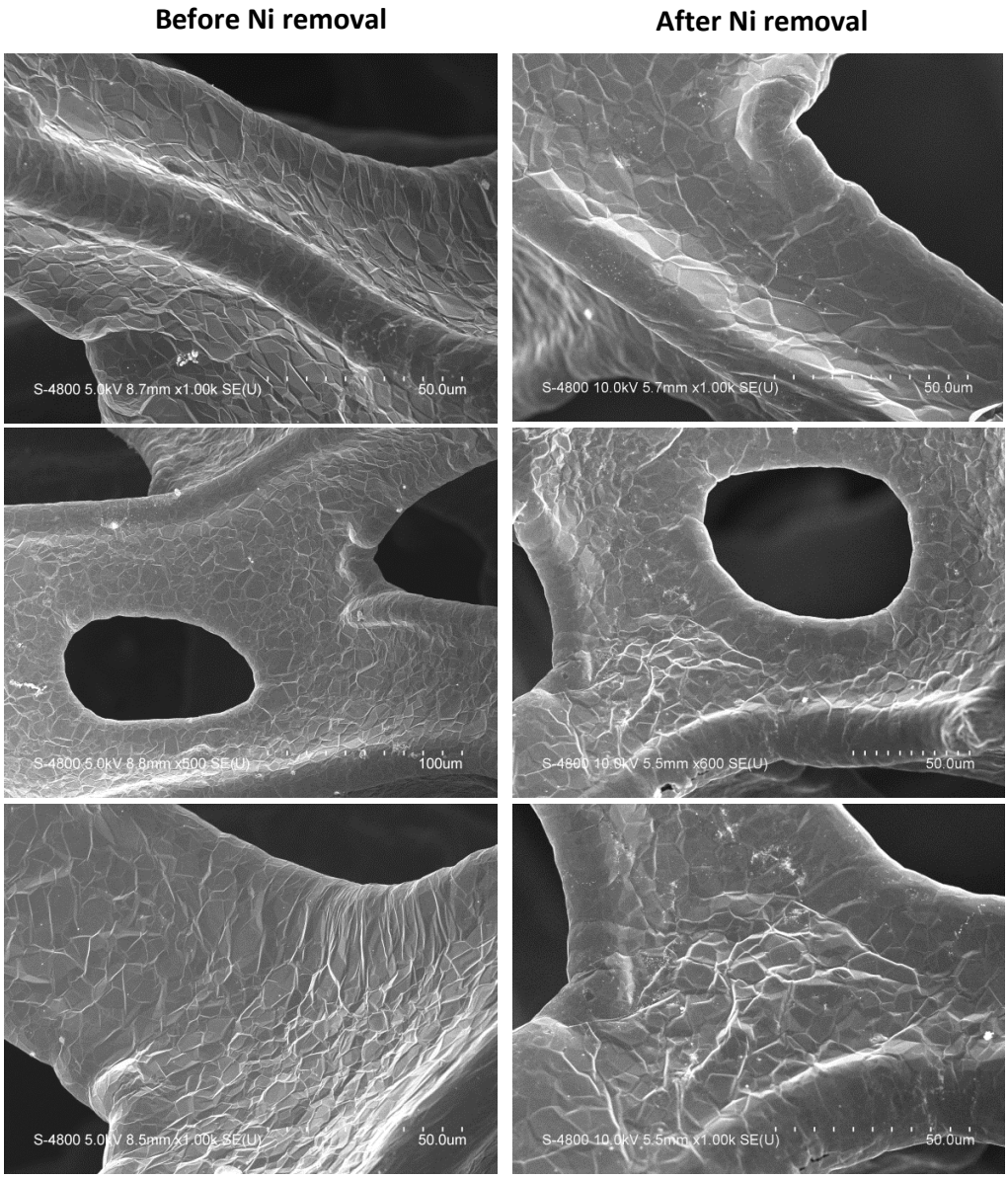

Figure S1: SEM micrographs of Gr foam before and after Ni removal.

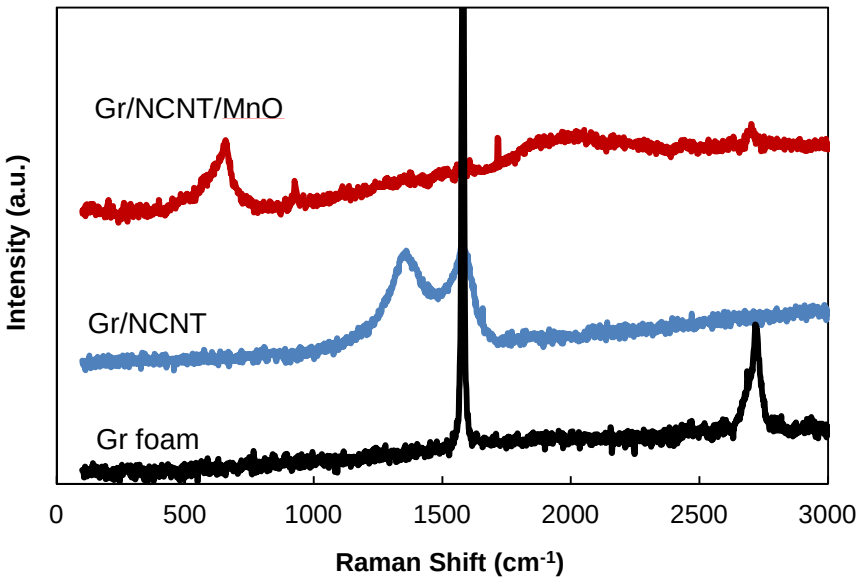

Figure S2: Raman spectra of Gr, Gr/NCNT and Gr/NCNT/MnO electrodes. Gr foam exhibits two peaks around 1570 and 2730 cm^{-1} corresponding to G and 2D bands, respectively.[4] The 2D peak in Gr foam spectrum is relatively wide and short compared to single-layer graphene which is a result of peak splitting due to the added forces from interactions between layers of AB-stacked graphene. In addition, the sharp and intense G-band indicates the presence of high crystalline graphitic carbon. The Raman spectra of Gr/NCNT, however, displays two peaks around 1370 and 1580 cm^{-1}, related to D and G bands, respectively. The high intensity D-band (I_D/I_G ~ 1) which is originated from atomic displacement and disorder induced features caused by lattice defect or distortion indicates a high amount of defects and disorders in NCNT. The Raman spectrum of Gr/NCNT/MnO shows a single peak at 657 cm^{-1} which can be correlated to the A_{1g} mode of Mn_3O_4 and is corresponding to the Mn-O stretching vibration of divalent manganese ions in the tetrahedral coordination.[5]

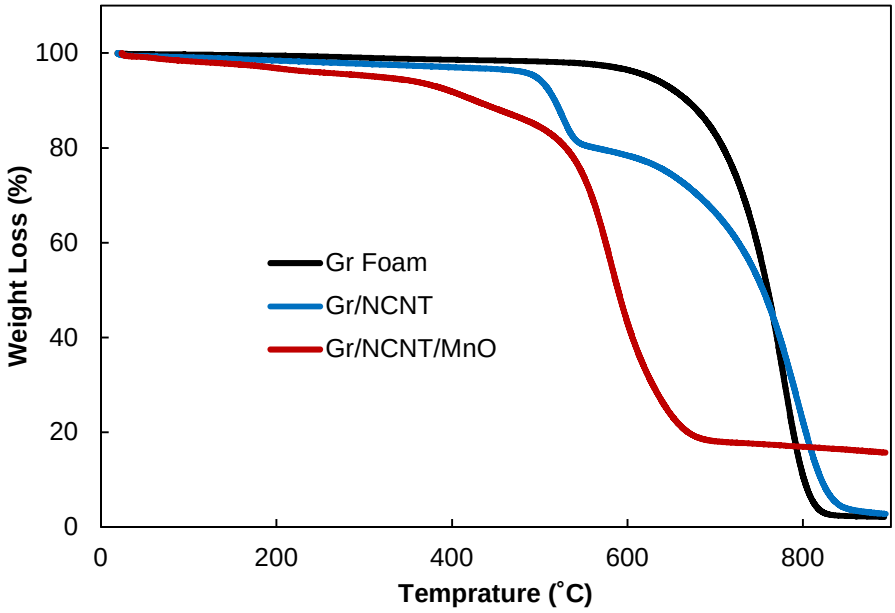

Figure S3: Thermogravimetric analysis (TGA) of Gr foam, Gr/NCNT and Gr/NCNT/MnO electrodes. The relative mass fraction of the electrode materials was examined by thermogravimetric analysis (TGA). Gr shows a significant mass reduction from 600 to 800 °C with the remaining mass of less than 3% which indicates the total removal of Ni through etching process. Gr/NCNT exhibits two consecutive reduction steps starting at 500 °C related to the NCNT decomposition followed by Gr removal. The mass fraction of NCNT can be estimated to be ~26% based on the first mass reduction step. Similar two-steps mass reduction curve was obtained for Gr/NCNT/MnO with ~17% remaining mass which is corresponding to the Mn_3O_4 mass fraction. The specific mass of Gr foam, Gr/NCNT and Gr/NCNT/MnO electrode materials were calculated based on the TGA results to be ~1.5, 1.9 and 2.2 mg cm^{-2}, respectively.

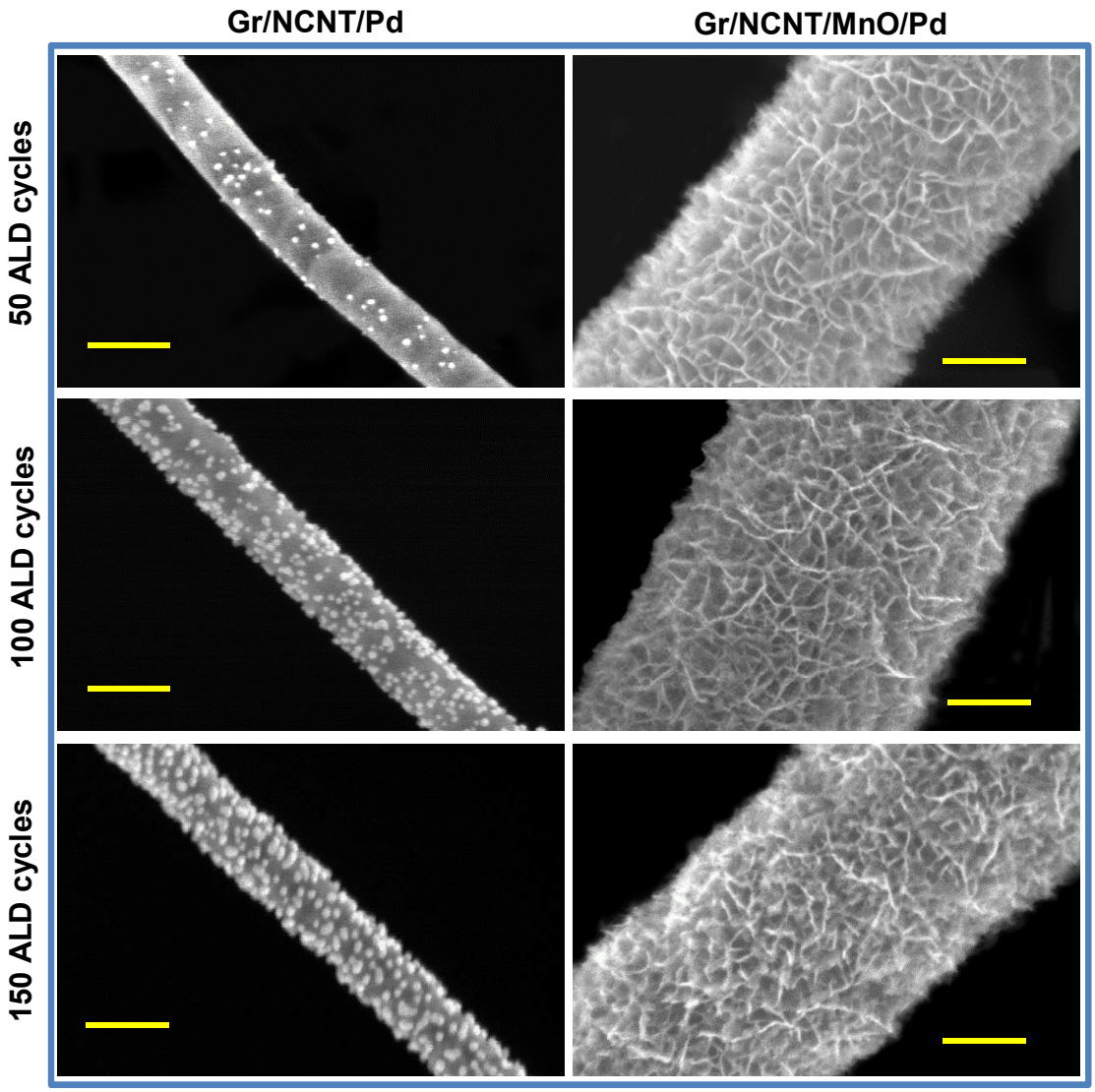

Figure S4: SEM micrographs of Gr/NCNT/MnO/Pd and Gr/NCNT/Pd with various ALD cycles. Pd is deposited as nanoparticles with dimensions less than 5 nm following 50 ALD cycles on NCNT surface. Both the size and density of the Pd nanoparticles increases with increasing the ALD cycle number to 100 and 150. Most of the NCNT surface is covered by Pd particles with a diameter of around 10 nm after 150 ALD cycles. However, Pd nanoparticles cannot be observed in the SEM micrographs of Mn3O4 surface even after increasing the ALD cycle number to 150.

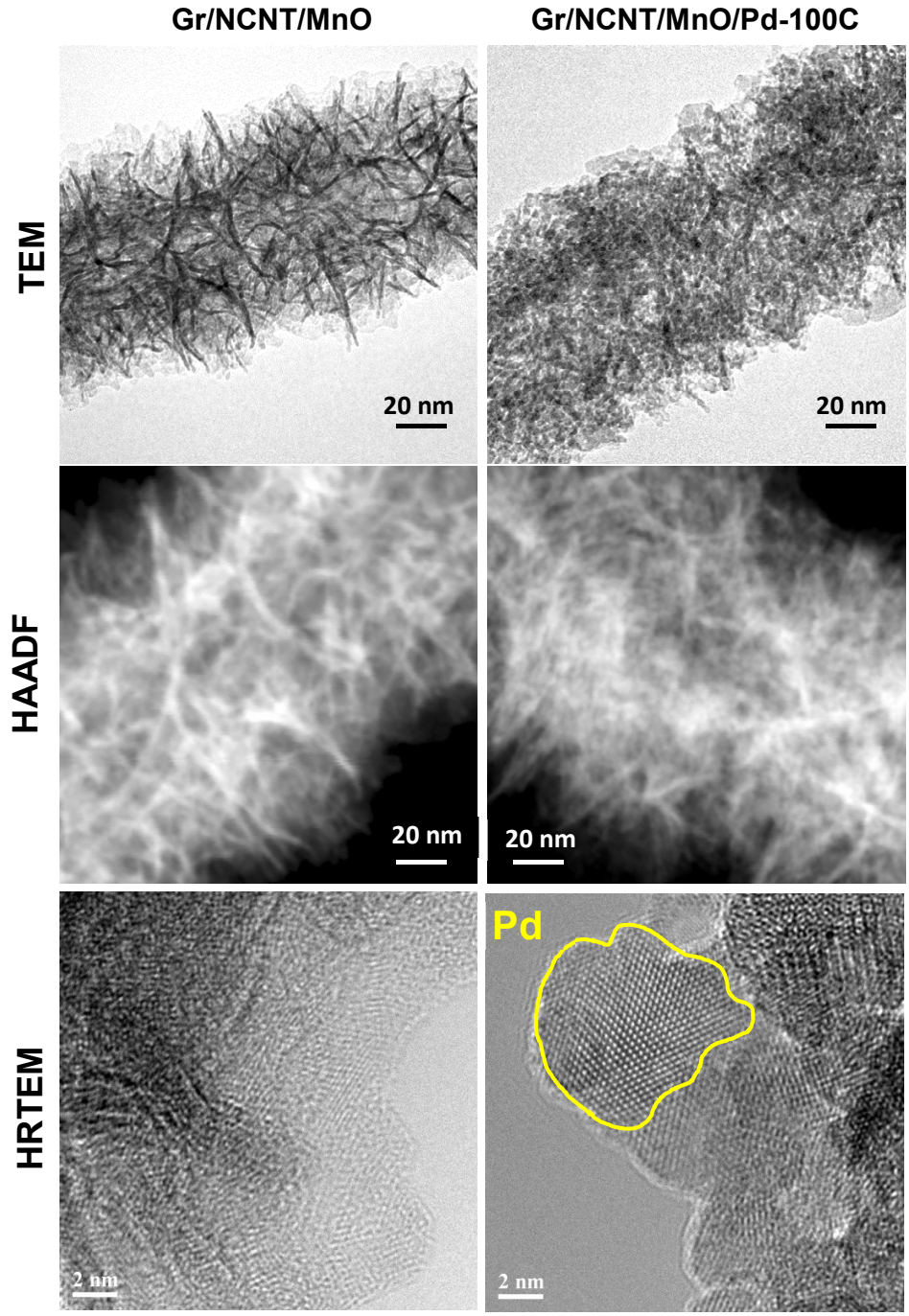

Figure S5: TEM, HAADF and HRTEM micrographs of Gr/NCNT/MnO electrode before and after 100 cycles of Pd deposition by ALD. Comparing the TEM images of the two electrodes reveals the presence of Pd nanoclusters on the Mn_3O_4 surface. High angle annular dark field (HAADF) image of the samples are also shown here. HAADF STEM images are formed by very high angle scattered

electrons which are sensitive to variations in the atomic number. HAADF STEM images of Pd-deposited electrodes exhibits a large number of high-contrast points which represent Pd nanoparticles. Moreover, HRTEM image of the Pd-deposited electrode displays a higher degree of crystallinity compared to the bare Mn_3O_4, resulting from a combination of Mn_3O_4 with highly ordered Pd.

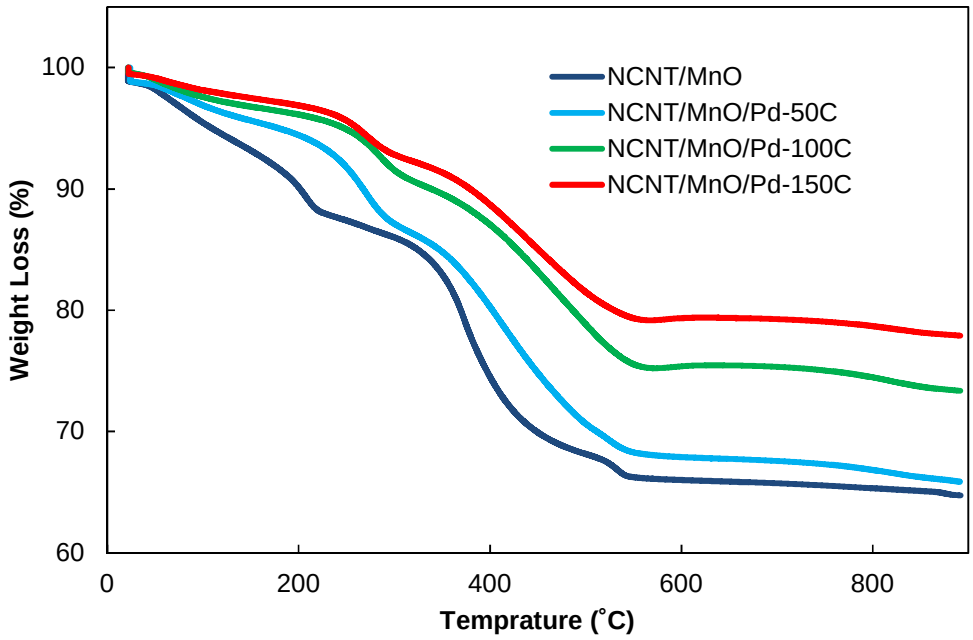

Figure S6: Thermogravimetric analysis (TGA) results of NCNT/MnO/Pd electrode materials before and after various number of Pd ALD cycles. Since the Gr foam is the dominant component in the total electrode weight, the TGA experiment for the Pd containing samples was conducted using powder-based samples (without Gr foam). The samples were prepared using NCNT as the starting materials using the same Pd ALD procedure. TGA of NCNT/MnO/Pd electrode materials with various number of Pd ALD cycles demonstrates increasing residual mass with increased number of ALD cycles, illustrating Pd deposition on the Mn_3O_4 surface. The rate of increased residual mass is lower for the first 50 ALD cycles, due to an initial nucleation process of the Pd ALD.[6] The Pd loading after 150 ALD cycles was calculated based on the TGA results to be ~0.05 mg cm^{-2}.

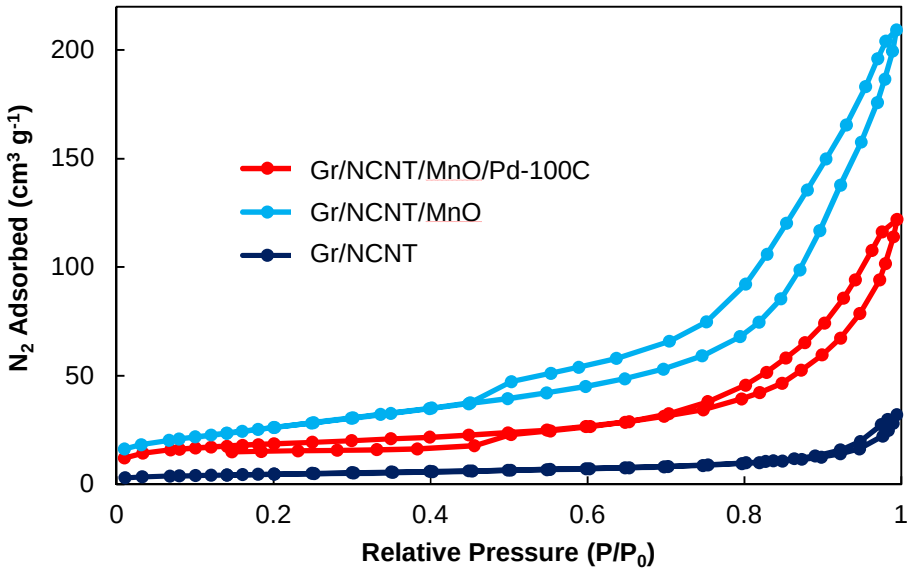

Figure S7: Nitrogen adsorption/desorption isotherms of Gr/NCNT, Gr/NCNT/MnO and Gr/NCNT/MnO/Pd-100C electrodes. The nitrogen adsorption/desorption isotherm of Gr/NCNT exhibits a type II diagram, indicating unrestricted monolayer-multilayer adsorption on a non-porous or macroporous adsorbent. Both Gr/NCNT/MnO and Gr/NCNT/MnO/Pd-100C electrodes show a type IV isotherm with a H3-type hysteresis loop at high p/p_0 which is indicative of capillary condensation within the mesopores.[7] It is also noteworthy that Gr/NCNT/MnO/Pd-100C shows a low pressure hysteresis which is due to the chemisorption of N_2 on the Pd surface.[7]

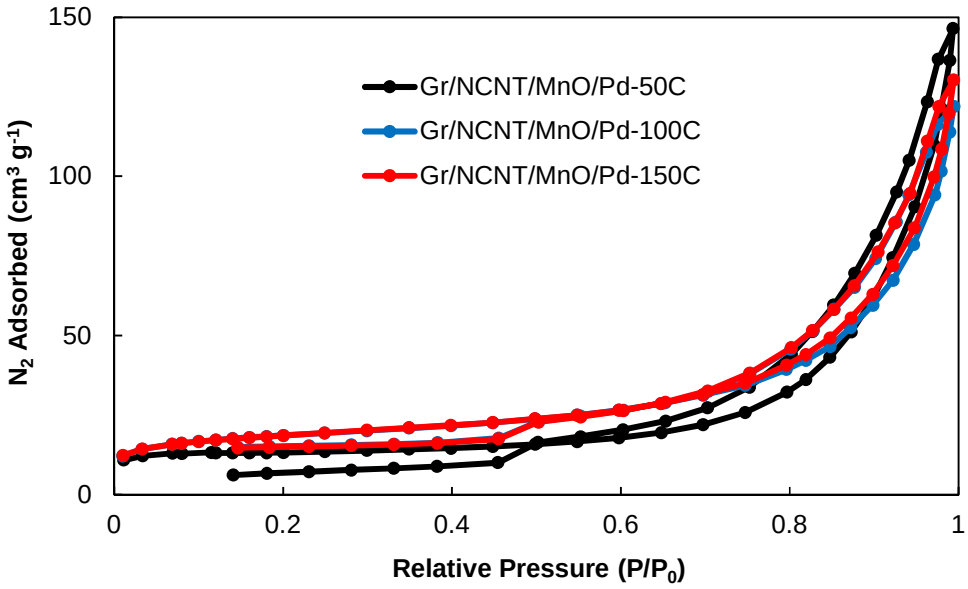

Figure S8: Nitrogen adsorption/desorption isotherms of Gr/NCNT/MnO/Pd-100C electrodes with various number of Pd ALD cycles. Similar adsorption/desorption isotherms were observed for the electrodes with 50 and 150 ALD cycles. The BET surface area of the electrodes was calculated to be 16.8, 95.0 and 64.1 m^2 g^{-1} for Gr/NCNT, Gr/NCNT/MnO and Gr/NCNT/MnO/Pd-100C, respectively (see also Table S1). The surface area of the electrode material significantly increases by precipitating mesoporous Mn_3O_4 on NCNT and then slightly decreases following Pd deposition. The decrease in BET surface area with increased number of Pd ALD cycles is due to the increased weight of the electrode as well as pore clogging by Pd deposition (see also Figure S9).

Table S1: Comparison of BET surface area of the synthesized electrodes.

Electrode material	BET Surface Area ($m^2 g^{-1}$)
Gr/NCNT	16.8
Gr/NCNT/MnO_2	95.5
Gr/NCNT/MnO_2/Pd-50C	65.5
Gr/NCNT/MnO_2/Pd-100C	64.1
Gr/NCNT/MnO_2/Pd-150C	43.8

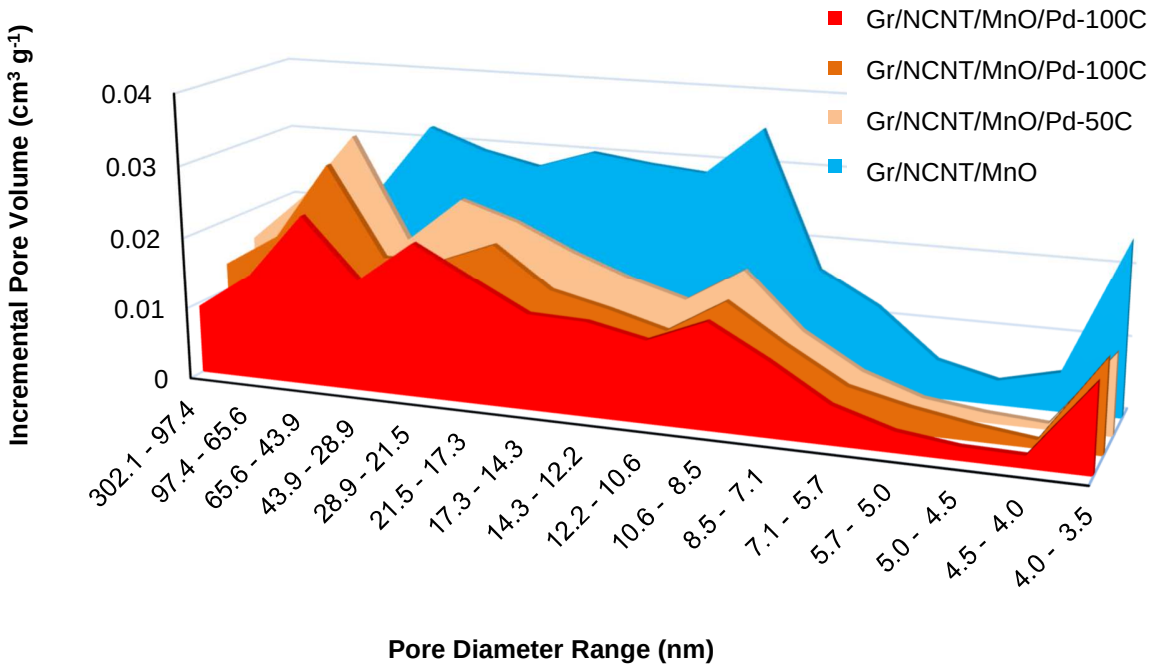

Figure S9: Pore volume distribution of Gr/NCNT/MnO in comparison with that of Gr/NCNT/MnO/Pd electrodes with various cycles of Pd deposition by ALD. The pore volume of the electrodes throughout the entire pore diameter range slightly decreases with increase of the ALD cycles, indicating the uniform Pd deposition onto the electrode porous structure. Moreover, the pore volume reduction is more significant after the first 50 ALD cycles especially in the pore diameter range of 10-50 nm which shows the partial clogging of the pores during the initial steps of the deposition process.

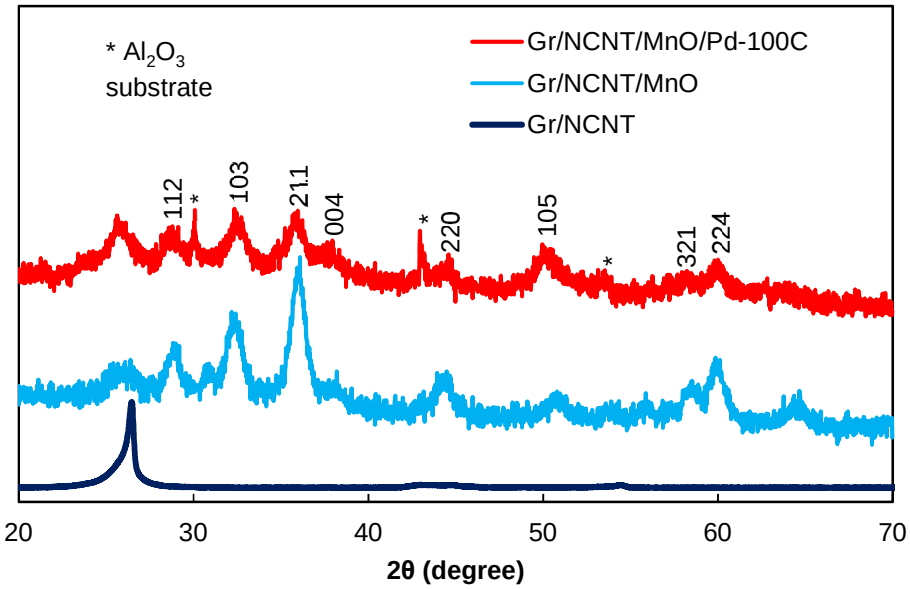

Figure S10: XRD pattern of Gr/NCNT, Gr/NCNT/MnO and Gr/NCNT/MnO/Pd-100C electrodes. Gr/NCNT present the typical graphitic peak at 2θ = 26˚. The additional peaks in the Gr/NCNT/MnO diffractogram matches well with tetragonal Mn_3O_4 (JCPDF ref. card No. 007-1841). No Pd peak was detected in the diffractogram of Gr/NCNT/MnO/Pd electrode, probably due to the low thickness of deposited Pd layer on Mn_3O_4 surface.

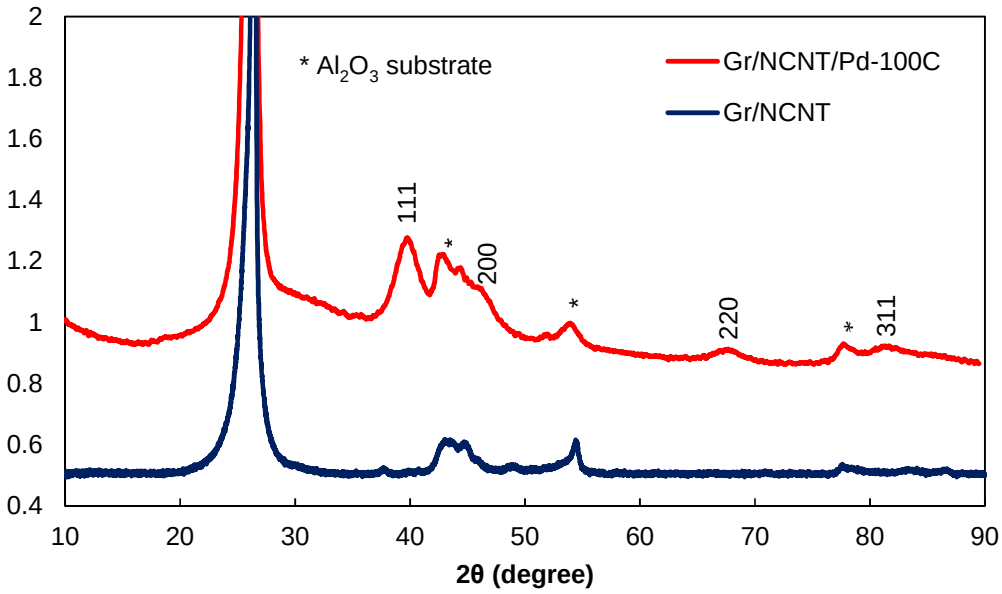

Figure S11: XRD pattern of Gr/NCNT and Gr/NCNT/Pd-100C electrodes. Pd peaks were detected on the Gr/NCNT/Pd electrode after 100 cycles of Pd ALD, confirming the formation of metallic Pd nanoparticles on NCNT. The XRD results are in good agreement with the direct observation of the electrode materials by SEM (Figure S4).

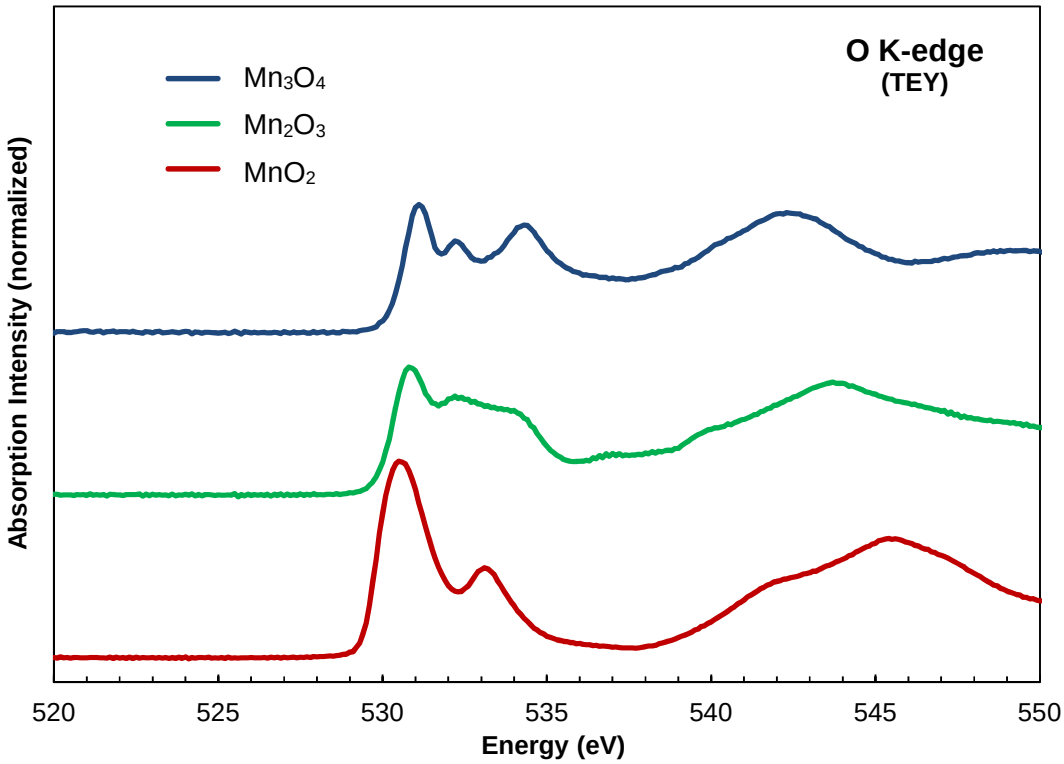

Figure S12: Normalized O k-edge XANES spectra of MnO_2 and Mn_2O_3 and Mn_3O_4 standard samples recorded under TEY mode. The fine structures on all standard sample spectra are in good agreement with previous reports.[8] The first feature around 530 eV in all oxides has been attributed to the electron transition from core O 1s to 2p hybridized with Mn 3d orbitals. This feature is split into 2 peaks (t_{2g} and e_g symmetry bands) in the case of MnO_2 and Mn_3O_4, while three peaks are present in the case of Mn_2O_3. The comparison of O K-edge spectra of standard manganese oxide samples with that of Gr/NCNT/MnO confirms the formation of Mn_3O_4.

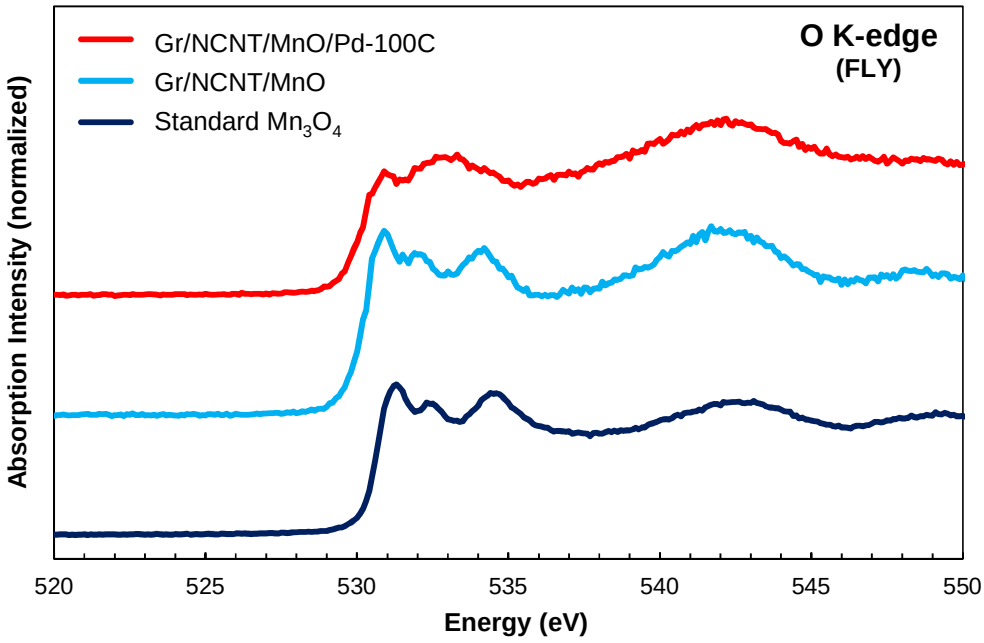

Figure S13: Normalized O k-edge XANES spectra of standard Mn_3O_4, Gr/NCNT/MnO and Gr/NCNT/MnO/Pd electrodes recorded under FLY mode. Appearance of similar features in both TEY (Figure 2b) and FLY modes indicates that both mesoporous Mn_3O_4 and Pd nanoclusters are composed of thin layers with uniform surface and bulk properties.

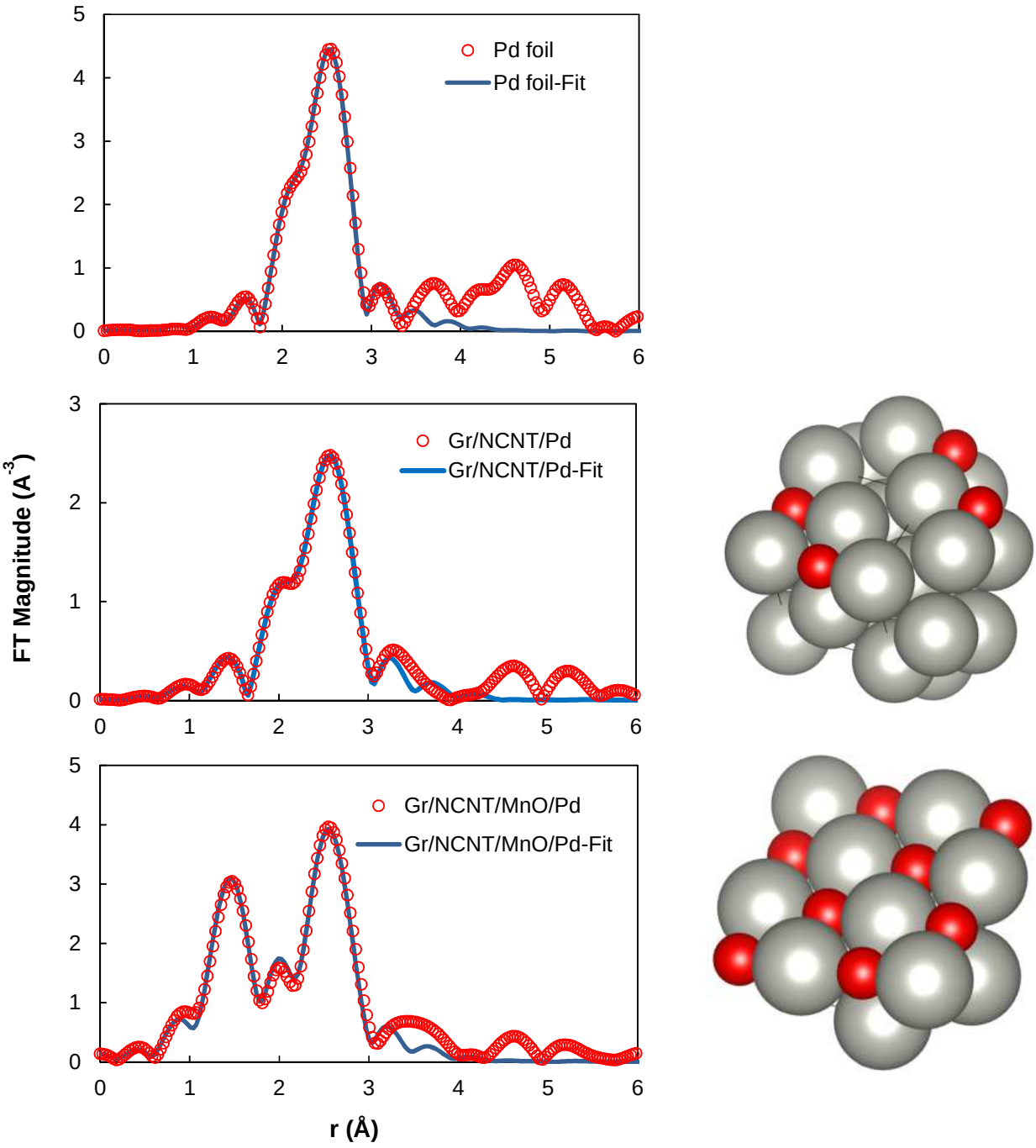

Figure S14: Fourier transform signal χ(R) of the experimental (circles) and calculated (solid line) Pd K-edge EXAFS χ(k) for standard Pd foil, Gr/NCNT/Pd and Gr/NCNT/MnO/Pd electrodes. The crystal structures of Pd/O used as fitting model are also given.

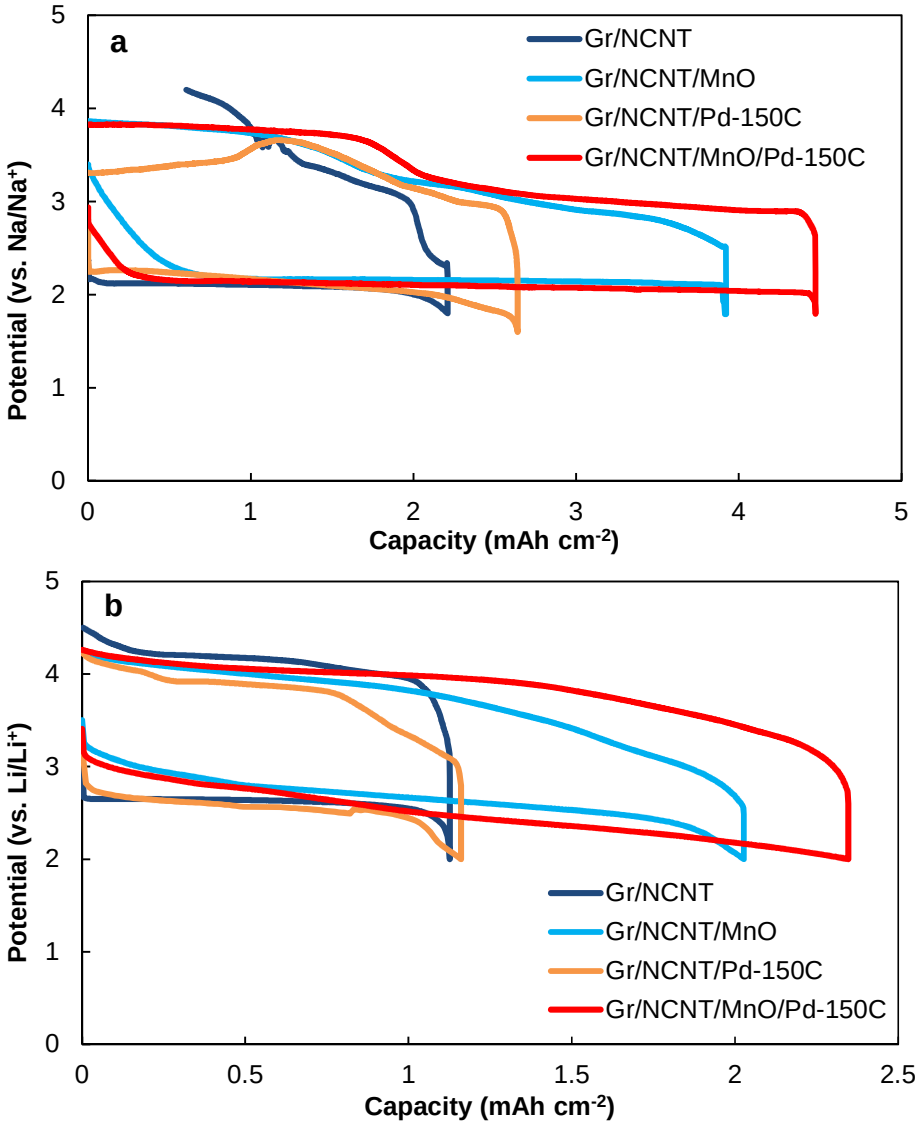

Figure S15: discharge/charge curves for Gr/NCNT, Gr/NCNT/MnO, Gr/NCNT/Pd-150C and Gr/NCNT/MnO/Pd-150C electrodes in Na- (a) and Li-O_2 (b) cells in full discharge capacity under a current density of 0.2 mA cm^{-2}. Gr/NCNT/MnO and Gr/NCNT/MnO/Pd electrodes show a significant increase in discharge capacity compared to Gr/NCNT and Gr/NCNT/Pd electrodes due to the enhanced surface area of the electrodes containing mesoporous Mn_3O_4. To compare the catalytic performance of the air electrodes, the discharge/charge curves restricted to the same discharge capacity were recorded which are demonstrated in Fig. 3.

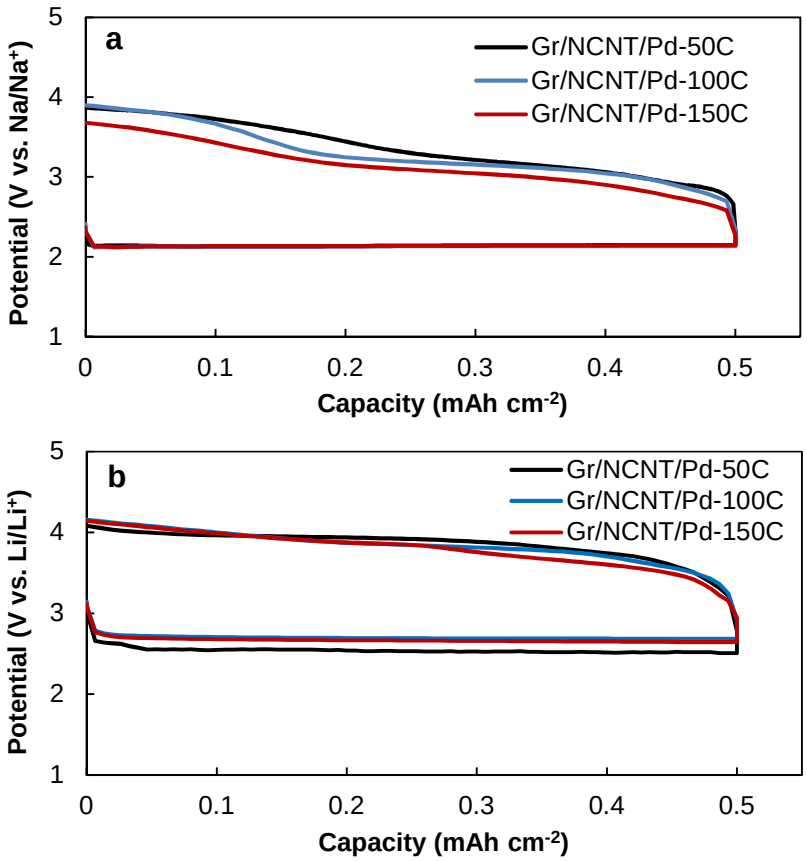

Figure S16: Discharge and charge curves of Gr/NCNT/Pd electrodes with various number of Pd ALD cycles for both Na- (a) and Li-O_2 (b) cells under a current density of 0.1 mA cm^{-2}. The charging overpotential in both cells negligibly decreases with increasing number of Pd ALD cycles, from 50 to 150. Since the Pd coverage on NCNT surface increases with ALD cycle number (see Figure S4), one would expect the overpotential of the cells to decrease accordingly. However, the growth mechanism of Pd on NCNT surface by ALD follows the Volmer-Weber mechanism.[9-11] By increasing the ALD cycles to 100 and 150, the initially formed nanoparticles grow in size to make larger Pd particles, resulting in similar electrocatalytic performance to 50 ALD cycles of Pd. In other words, the increase of ALD cycles to 100 and 150 increases the bulk Pd which does not contribute to reducing the overpotential during OER. The slight improvement in charging overpotential from 50 to 150 ALD cycles, however, can be attributed to the formation of new nucleation sites formed during increased number of ALD cycles.

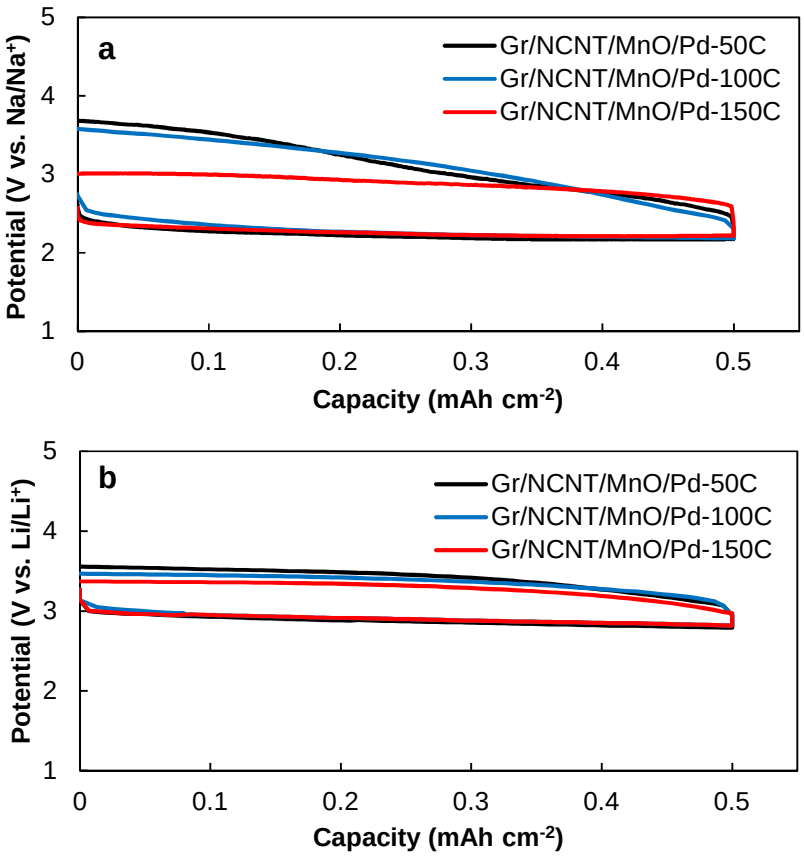

Figure S17: Discharge and charge curves of Gr/NCNT/MnO/Pd electrodes with various number of Pd ALD cycles in both Na- (a) and Li-O_2 (b) cells under a current density of 0.1 mA cm^{-2}. Unlike Gr/NCNT/Pd, Gr/NCNT/MnO/Pd electrodes demonstrate a stronger correlation between reduction in charging overpotential and ALD cycle number. The different correlation between Pd ALD cycles on NCNT and Mn_3O_4 surfaces with electrochemical response of the electrodes is related to the distinct growth mechanisms occurring on these surfaces. As mentioned earlier, nucleation originates at defect sites on the NCNT surface and produces island-like nanoparticles. However, the Mn_3O_4 surface provides a rich number of defect sites for Pd nucleation resulting in the formation of nanoclusters and/or atomic films. Increasing the ALD cycles on NCNT formed bulky Pd particles, while multiple ALD cycles on Mn_3O_4 results in planar expansion of Pd nanoclusters to make a thin film while also increasing the density of active Pd. Therefore, an increase in the number of ALD cycles on Mn_3O_4 results in enhanced OER performance due to higher coverage of Pd nanoclusters.

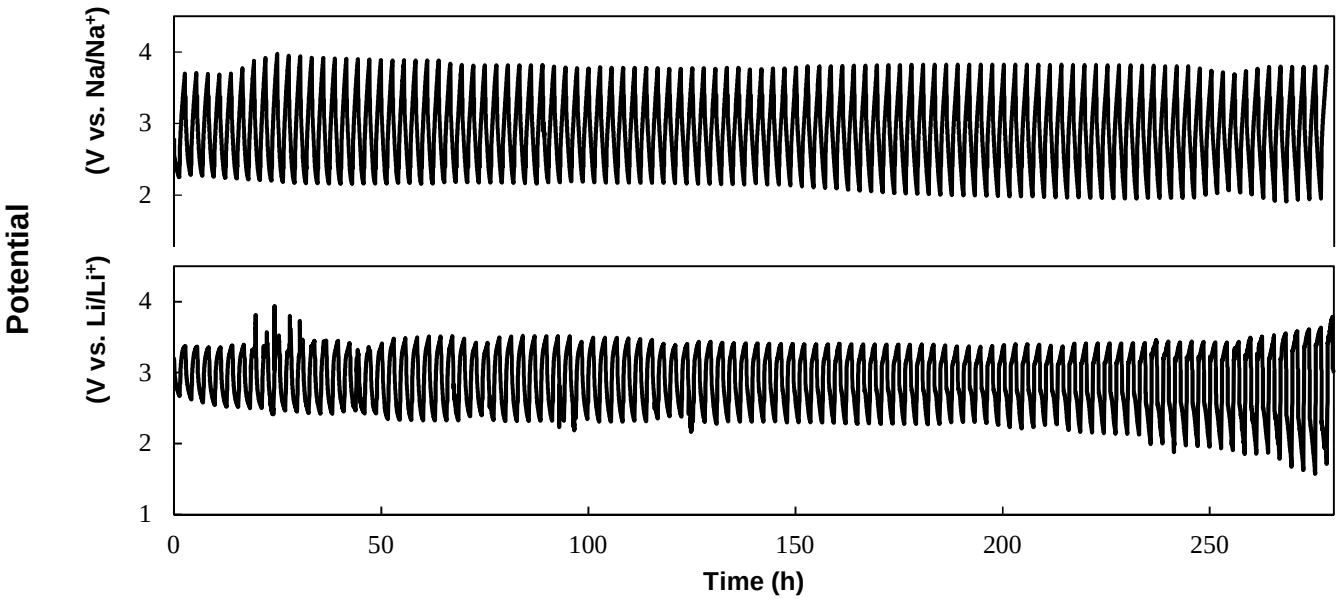

Figure S18: The chronopotentiaogram curves of the consecutive discharge and charge test of Gr/NCNT/MnO/Pd-150C electrode in bor Na- and Li-O_2 cells for the data shown in Figure 3c and d.

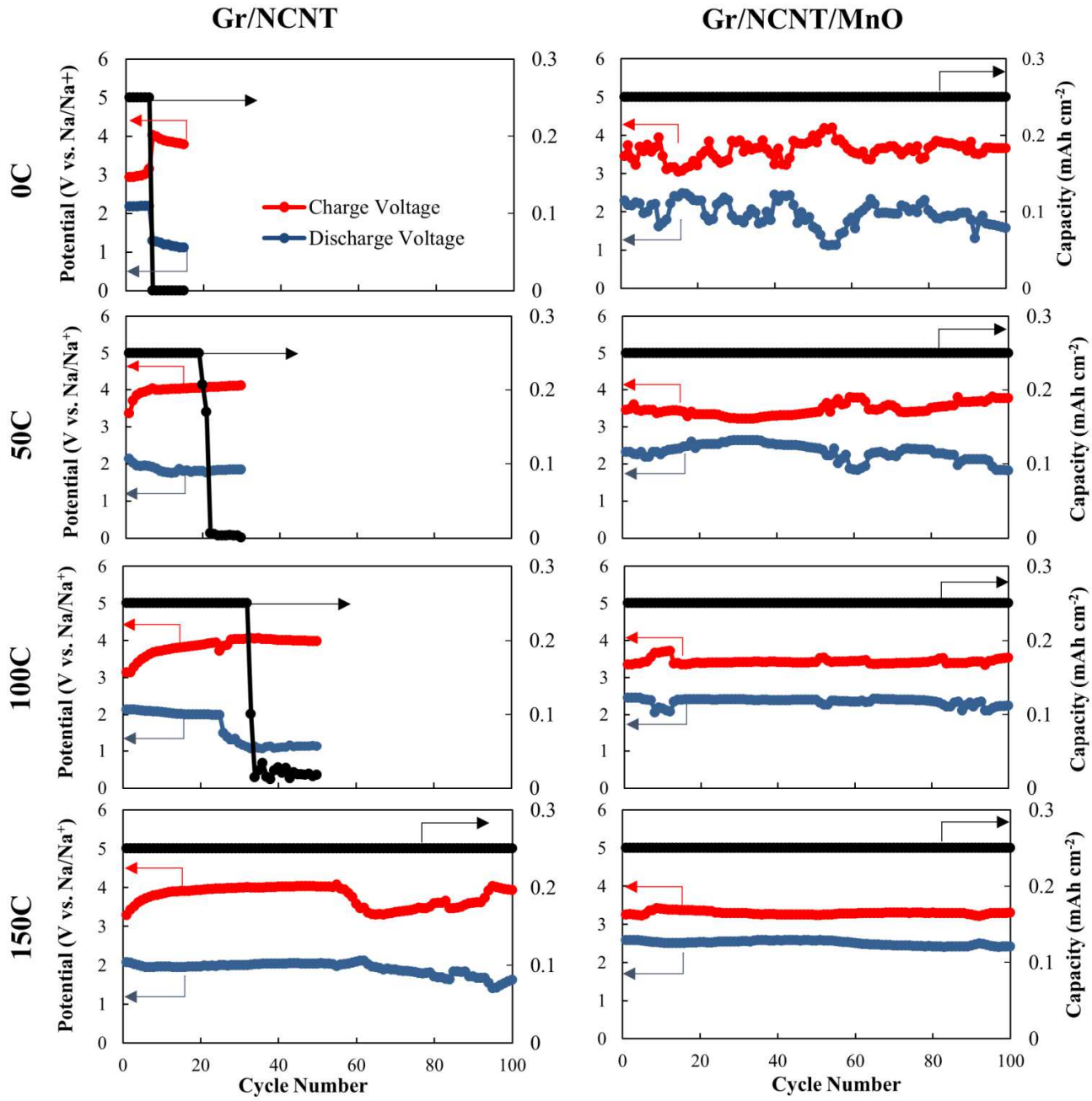

Figure S19: The cycling performance of Gr/NCNT/Pd and Gr/NCNT/MnO/Pd electrodes with various cycles of Pd deposition by ALD in Na-O_2 cell.

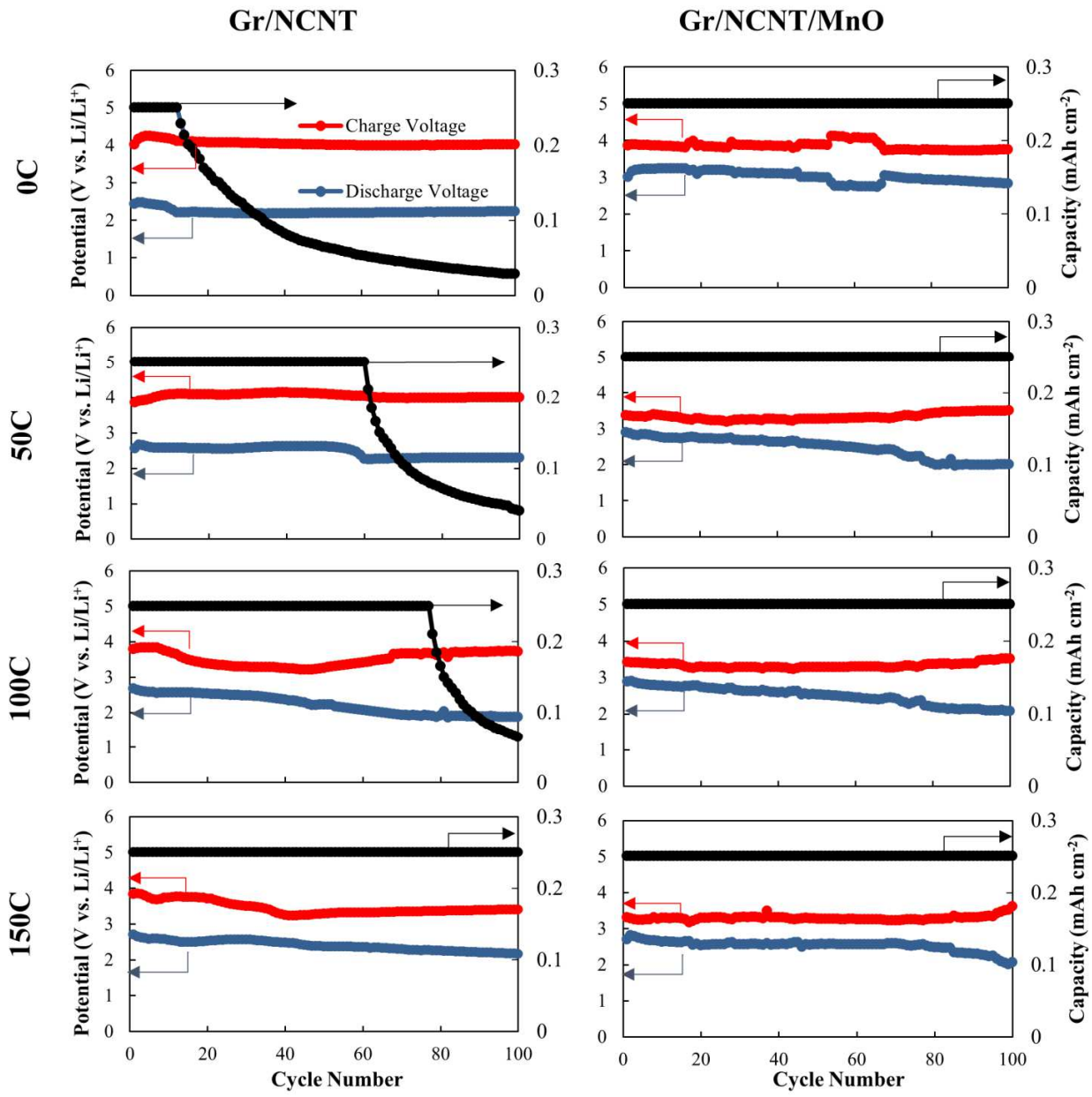

Figure S20: The cycling performance of Gr/NCNT/Pd and Gr/NCNT/MnO/Pd electrodes with various cycles of Pd deposition by ALD in Li-O_2 cell.

The cycling performance:

The cycling performance of the cells is obviously improved with increased number of Pd ALD cycles for Gr/NCNT electrode. The improved cycle life of the cells can be attributed to the enhanced charge transfer at Pd/NCNT interface as well as shielding effect of Pd nanoparticles over the carbon surface to prevent carbonate formation.

In addition, both Na- and Li-O_2 cells exhibit 100 consecutive discharge and charge cycles using Gr/NCNT/MnO electrode, probably due to the high surface area mesoporous structure of the electrode. The high surface area electrode decreases the thickness of the discharge products on the air electrode surface and decreases the charging overpotential of the cell by improving the charge and mass transfer through the discharge product layer. In addition, the charging overpotential of the cells decreases with increased number of Pd ALD cycles for both Gr/NCNT and Gr/NCNT/MnO electrodes which is likely due to the enhanced charge transfer at Pd/air electrode interface.

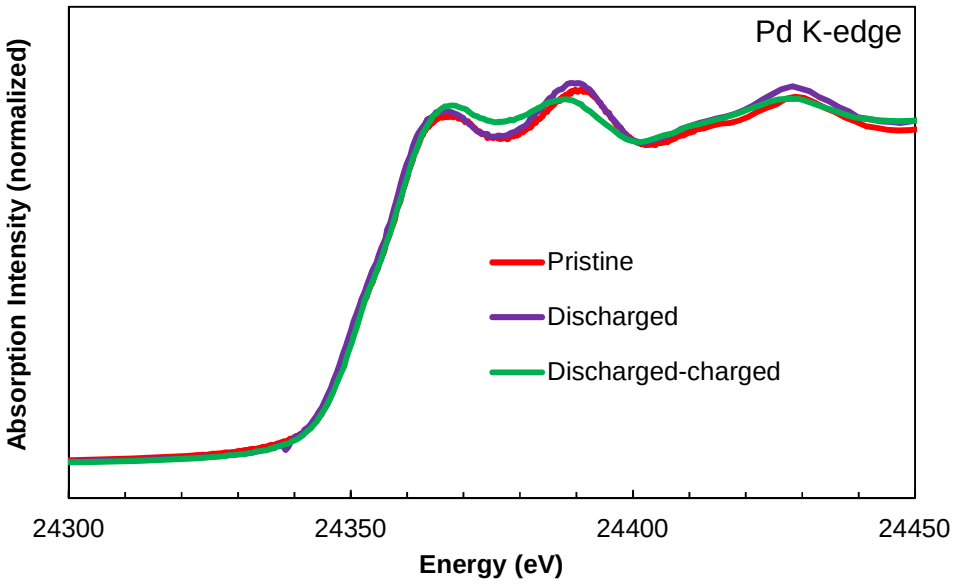

Figure S21: The Pd K-edge XANES spectra of Gr/NCNT/Pd electrode before 1st discharge, after 1st discharge and after 1st discharge/charge cycle. Gr/NCNT/Pd electrode shows same absorption edge at different discharge and charge cycles, suggesting that electron exchange is not happened between Pd nanoparticles and carbon substrate. However, Pd nanoparticles on NCNT exhibit a structural change in EXAFS spectra, probably due to the adsorption of oxygen onto the Pd surface.

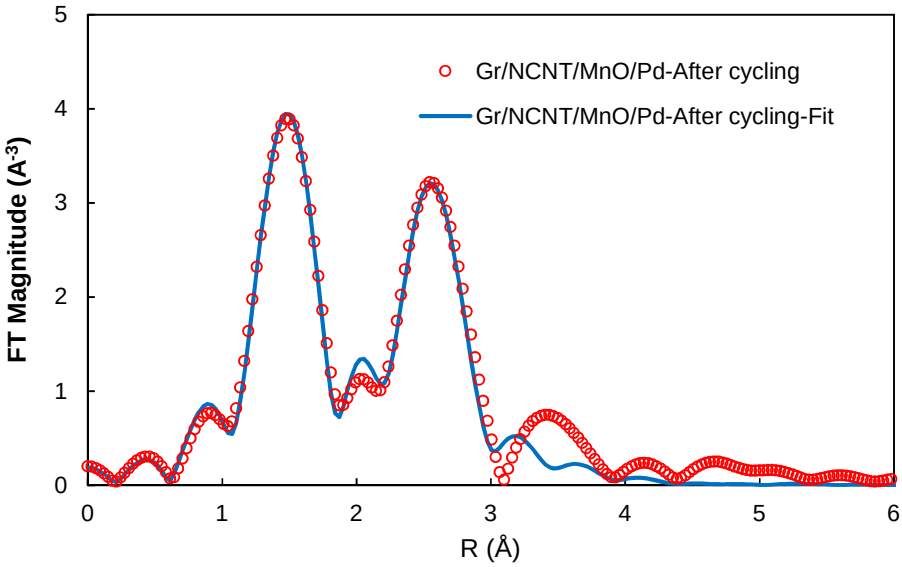

Figure S22: Fourier transform signal χ(R) of the experimental (circles) and calculated (solid line) Pd K-edge EXAFS χ(k) for Gr/NCNT/MnO/Pd electrode before and after 100 cycles in a Na-O_2 cell.

Table S2: The structural parameters obtained from curve fitting depicted in Figure S22.

	Pd-Pd Coordination	**Pd-O Coordination**	**Pd-Pd Debye-Waller factor (Å²)**	**Pd-O Debye-Waller factor (Å²)**
Gr/NCNT/MnO/Pd	3.581	2.188	7.52×10^{-3}	4.91×10^{-3}
Gr/NCNT/MnO/Pd-Cycled	2.425	2.385	6.51×10^{-3}	2.26×10^{-3}

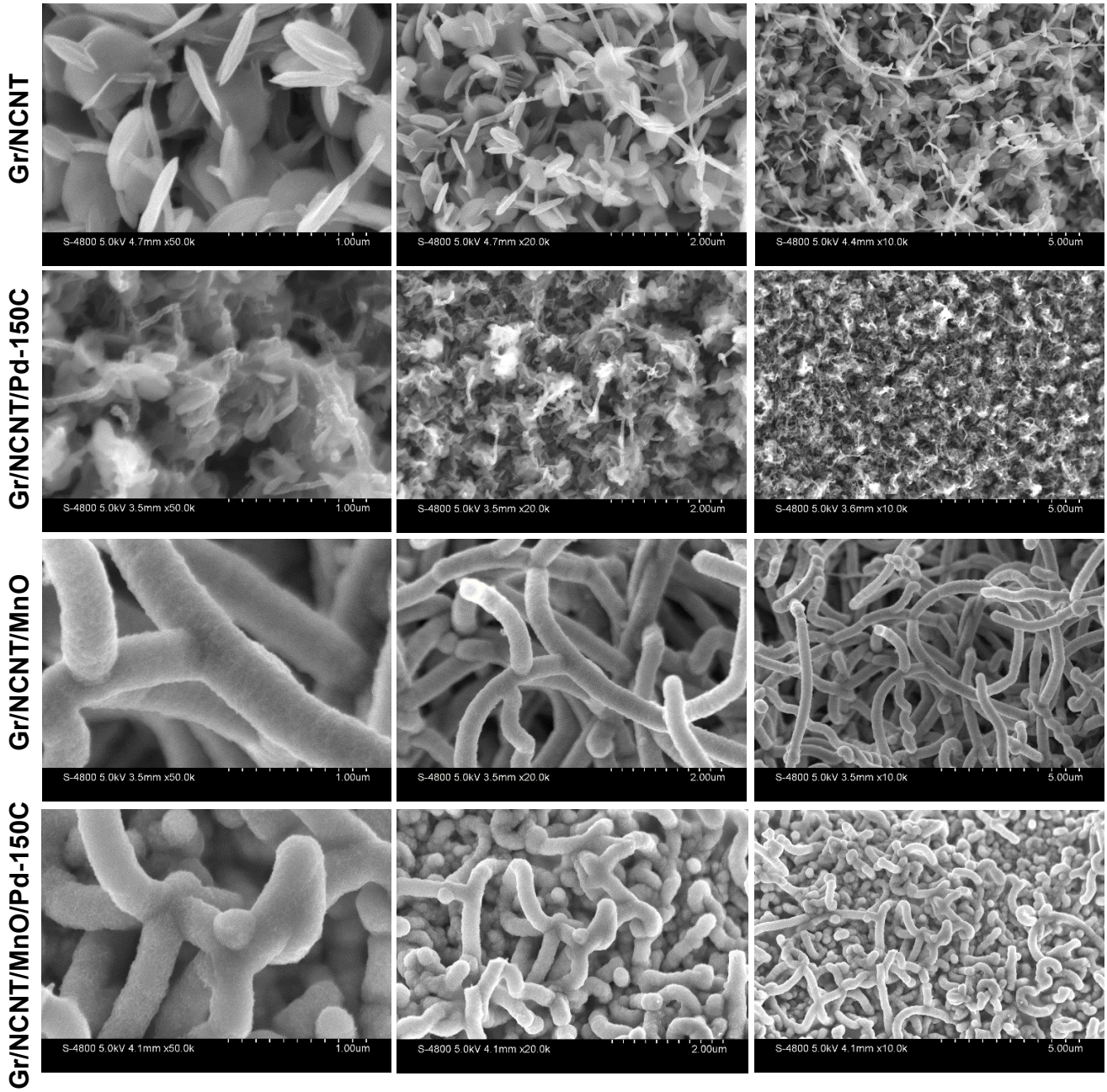

Figure S23: Morphology of the discharge products in Li-O_2 cell using various air electrodes after discharge to 1.0 mAh cm^{-2} under a current density of 0.1 mA cm^{-2}.

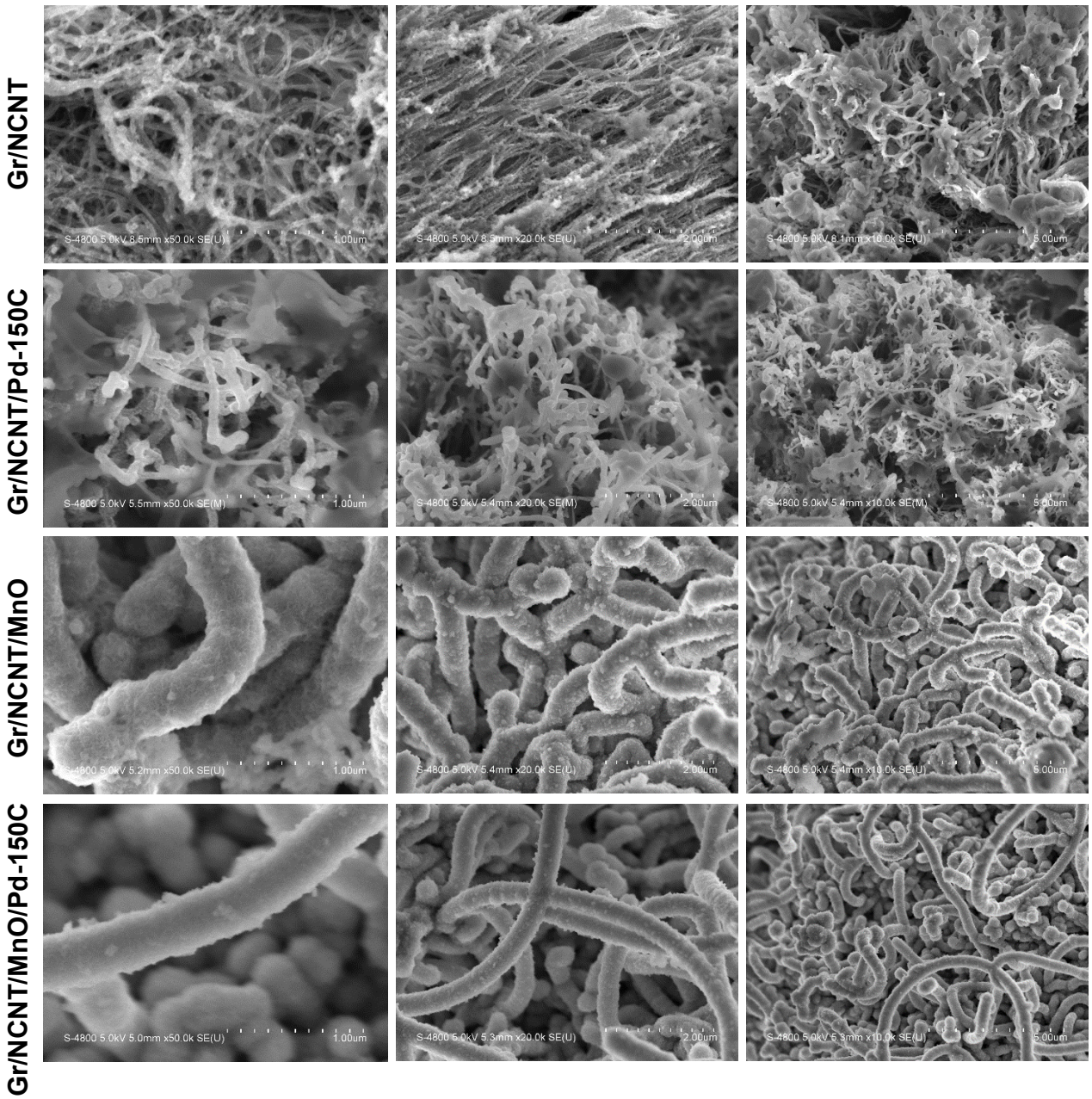

Figure S24: Morphology of the discharge products in Na-O_2 cell using various air electrodes after discharge to 1.0 mAh cm^{-2} under a current density of 0.1 mA cm^{-2}.

References

1. Z. P. Chen, W. C. Ren, L. B. Gao, B. L. Liu, S. F. Pei and H. M. Cheng, *Nat Mater*, 2011, **10**, 424-428.
2. H. Yadegari, M. N. Banis, B. Xiao, Q. Sun, X. Li, A. Lushington, B. Wang, R. Li, T.-K. Sham, X. Cui and X. Sun, *Chem. Mater.*, 2015, **27**, 3040-3047.
3. Y. Chen, Y. Zhang, D. S. Geng, R. Y. Li, H. L. Hong, J. Z. Chen and X. L. Sun, *Carbon*, 2011, **49**, 4434-4442.
4. A. C. Ferrari and D. M. Basko, *Nat Nanotechnol*, 2013, **8**, 235-246.
5. Z. Y. Tian, P. M. Kouotou, N. Bahlawane and P. H. T. Ngamou, *J. Phys. Chem. C*, 2013, **117**, 6218-6224.
6. D. N. Goldstein and S. M. George, *Thin Solid Films*, 2011, **519**, 5339-5347.
7. K. S. W. Sing, *Pure Appl. Chem.*, 1982, **54**, 2201-2218.
8. H. Kurata and C. Colliex, *Physical Review B*, 1993, **48**, 2102-2108.
9. S. M. George, *Chem. Rev.*, 2010, **110**, 111-131.
10. M. J. Weber, A. J. M. Mackus, M. A. Verheijen, V. Longo, A. A. Bol and W. M. M. Kessels, *J. Phys. Chem. C*, 2014, **118**, 8702-8711.
11. A. J. M. Mackus, M. J. Weber, N. F. W. Thissen, D. Garcia-Alonso, R. H. J. Vervuurt, S. Assali, A. A. Bol, M. A. Verheijen and W. M. M. Kessels, *Nanotechnology*, 2016, **27**, 034001.